Bis[1]benzothieno[1,4]thiaborins as a Platform for BODIPY Singlet Oxygen Photosensitizers

Paulina H. Marek-Urban,[a,b]* Karolina A. Urbanowicz,[a] Karolina Wrochna,[a] Piotr Pander,[c,d,e] Agata Blacha-Grzechnik,[c,d] Henning R. V. Berens,[f] Krzysztof Woźniak,[b] Thomas J. J. Müller,[f] Krzysztof Durka[a]*

[a]   P. H. Marek-Urban, K. A. Urbanowicz, K. Wrochna, Dr. K. Durka
        Faculty of Chemistry,
        Warsaw University of Technology
        Noakowskiego 3, 00-664 Warsaw, Poland
        E-mail: krzysztof.durka@pw.edu.pl (K. D.); paulina.marek.dokt@pw.edu.pl (P. M.-U.)
        Homepage: http://lulinski.pw.edu.pl
[b]   P. H. Marek-Urban, Prof. K. Woźniak
        Department of Chemistry,
        University of Warsaw
        Żwirki i Wigury 101, 02-089 Warsaw, Poland
[c]   Dr. P. Pander, Dr. A. Blacha-Grzechnik
        Faculty of Chemistry
        Silesian University of Technology
        Strzody 9, 44-100 Gliwice, Poland
[d]   Dr. P. Pander, Dr. A. Blacha-Grzechnik
        Centre for Organic and Nanohybrid Electronics,
        Silesian University of Technology
        Konarskiego 22B, 44-100 Gliwice, Poland
[e]   Dr. P. Pander
        Department of Physics,
        Durham University
        South Road, Durham DH1 3LE, UK
[f]   Dr. H. R. V. Berens, Prof. Dr. T. J. J. Müller
        Institut für Organische Chemie und Makromolekulare Chemie
        Heinrich-Heine-Universität Düsseldorf
        Universitätsstrasse 1, D-40225 Düsseldorf, Germany

   Supporting information for this article is given via a link at the end of the document.

Abstract: A synthetic approach to two regioisomeric π-electron extended [1,4]thiaborins anellated with two benzothiophene units was developed. Obtained boracycles exhibit different electronic properties of the central thiaborin ring reflected in their different aromatic characters, boron Lewis acidity and UV-Vis spectroscopic behavior. Thiaborins were converted to boron dipyrromethene (BODIPY) complexes. Their emission spectra exhibit two distinct bands resulting from ^{1}LE and ^{1}CT transitions. Strong near infrared phosphorescence in Zeonex thin films at 77 K indicates efficient intersystem crossing and formation of triplet states. Separation of HOMO and LUMO orbitals between boracyclic and BODIPY moieties facilitates the electron transfer to a ^{1}CT state followed by a transition to the ^{3}LE triplet state located on the ligand. These unique properties of *spiro* thiaborin-BODIPY complexes were explored for their application as singlet-oxygen photosensitizers. They show excellent photocatalytic performance with singlet oxygen quantum yields reaching 77% and full conversion of the model organic substrate achieved after 1.5 h with only 0.05% mol catalyst load.

Introduction

Thiophene-based π-conjugated materials have been extensively studied due to their tunable and diverse optoelectronic properties which spread out their applications into different areas of organic electronics, including organic light-emitting diodes (OLEDs),[1–3] dye-sensitized solar cells (DCCSs),[4–7] organic field-effect transistors (OFETs)[8,9] and organic photovoltaics (OPVs).[8,10,11] Thiophene is characterized by outstanding electron and hole transport properties, whilst remaining chemically and thermally resistant. As the device performance ultimately originates from the molecular properties, the incorporation of electron-rich atoms such N, P or S emerged as an attractive method to modulate the electronic structure of the material.[12–17] For instance, electron-rich heterocycles such as phenothiazines[6,18,19] and their dithienyl congeners, namely dithieno[1,4]thiazines,[20–23] have attracted a of lot interest due to their low oxidation potentials and reversibility of the redox processes, as well as NIR luminescence.[24] Furthermore, the expansion of the dithieno[1,4]thiazines to the pentacyclic bis[1](benzothienylo)[1,4]thiazine (**BBTT**, **Scheme 1**) strongly favors luminescent behavior.[25–28]

On the other hand, incorporation of an electron deficient atom such as boron atom into a π-electron conjugated system results in a significant lowering of the LUMO level which leads to electron-deficient characteristics.[29–38] Fused triarylboranes are thus commonly utilized as dopants for electron-transporting materials,[39–43] anion-receptors,[44–48] Lewis acid catalysts,[49–60] and light-emitting materials.[61–67] From the known structures of boracyclic compounds,[44,68] boron-containing thiophene-fused systems are an especially fascinating class of functional materials thanks to their unique optical properties derived from the electron-accepting character of boron atom combined with electron-conducting and polarizable thiophene units.[69] Yamaguchi reported a pioneering work in this subject in 2011 with the first
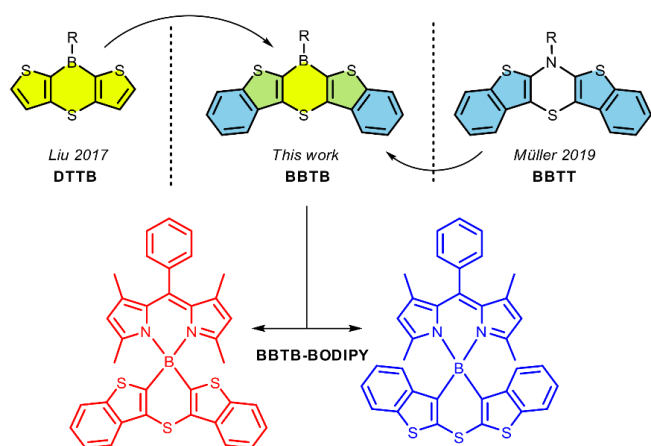
Scheme 1. Molecular design of bis[1]benzothieno[1,4]thiaborins and their BODIPY complexes.

successful synthesis of thiophene-based boroles.[70] They showed that thiophene rings enhance the antiaromatic character of the 5-membered boraheterocycle. In the following years, Piers and co-workers obtained light-emitting bis[1]benzothieno[1,4]diborins containing two boron atoms in the 6-membered central ring.[71] Later, thiophene-fused analogues of diboraanthracenes were exploited as UV irradiation sensors.[72] Subsequently, 7-membered borepins fused with thiophene rings were introduced by Tavor and further studied by Ohshita, Adachi, and others.[73–77] Finally, Liu and co-workers reported successful synthesis of two isomeric dithieno[1,4]thiaborins (**DTTBs**, **Scheme 1**),[78] boron-based analogues of dithieno[1,4]thiazines.

Although the tri-coordinate thienyl-fused boracycles emerged as promising building blocks for optoelectronic devices, reports concerning their chelate boron complexes are sparse.[79] Recently, we have demonstrated that *spiro*-organoboron complexes, *i.e.* where a tetracoordinate boron atom acts as a node connecting borafluorene and (N,O) or (N,N)-chelate ligand, can be utilized as efficient photosensitizers for generation of singlet oxygen.[80] Separation of the HOMO and LUMO orbitals localized on orthogonally aligned borafluorene and ligand moieties allows for efficient intersystem crossing to triplet state *via*

spin-orbit charge transfer mechanism (SOCT-ISC).[81–83] Subsequent energy transfer from the triplet state of the photosensitizer to triplet oxygen ($^3O_2$) generates singlet oxygen ($^1O_2$). The latter, is a powerful oxidant used for selective oxidation of small-molecule organic substances[84,85] or degradation of biomolecules. It was successfully used for anticancer photodynamic therapy (PDT),[86–92] photodynamic antimicrobial inactivation,[93–97] degeneration of chemical toxins,[98,99] and water purification.[100,101] We have found that the photocatalytic activity of borafluorene-based dyads outperforms the commercially used photocatalysts such as Rose Bengal (RB) or 5,10,15,20-tetraphenylporphyrin (TPP), making them promising candidates for new generation of heavy atom-free photosensitizers.

Herein, we present the synthesis of two regioisomeric bis[1]benzothieno[1,4]thiaborins (**BBTBs**), which can be considered as the electron-deficient congeners of the electron-rich anellated S,N-heteropentacenes such as **BBTTs** or,[102] alternatively, dibenzo extended analogues of **DTTBs** (**Scheme 1**).[78] We have performed comprehensive studies of the basic molecular and structural properties of the newly obtained bis[1]benzothieno[1,4]thiaborins and used them as scaffolds for the construction of tetracoordinate boron dipyrromethane complexes (**BBTB**-**BODIPY**). We have shown that the optical properties of BODIPY complexes are derived from electronic properties of the BBTB cores. Finally, **BBTB**-**BODIPY** were utilized as efficient singlet oxygen photosensitizers in photocatalysis.

Results and Discussion

Synthesis. We have obtained two BBTB regioisomers differing by the mode of annulation of the benzothiophene units with respect to the central [1,4]thiaborin heterocycle. Following the nomenclature introduced for **BBTTs**,[25,28] the isomer with sulfur atoms located on the same side of the molecule as central sulfur atom is referred to as *syn-syn*-**BBTB**, while the other isomer is referred to as *anti-anti*-**BBTB**. The abbreviation is supplemented by the functionalization type at the boron atom specified after a dash (OH, Mes, Cl or BODIPY). As shown in **Scheme 2** both
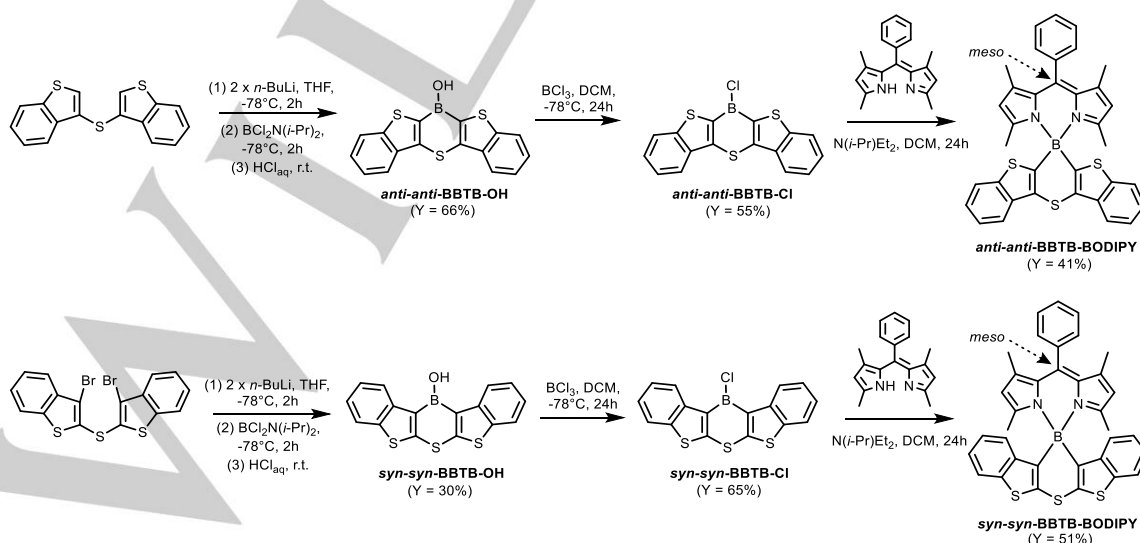
Scheme 2. Synthesis of **BBTB-OH** and respective **BBTB-BODIPY** complexes.

BBTB regioisomers were obtained from respective bis(benzothiophenyl)sulfides. Synthesis of *syn-syn*-**BBTB-OH** started from bis(benzo[b]thiophen-3-yl)sulfide, which was selectively deprotonated with *n*-BuLi. Obtained dilithium intermediate was treated with $BCl_2N(i\text{-}Pr)_2$ and subsequently hydrolyzed with 1M HCl. The *anti-anti*-**BBTB-OH** was prepared from bis(3-bromobenzo[b]thiophen-2-yl)sulfide subjected to a double Br-Li exchange reaction with *n*-BuLi. Then, one equivalent of $BCl_2N(iPr)_2$ was added followed by hydrolysis to give the final compound as a white solid. Both BBTBs were isolated in a form of borinic acid (**BBTB-OH**). Structures of obtained compounds were confirmed with ^{1}H, ^{11}B, ^{13}C NMR spectroscopy, X-ray crystallography, HR-MS and elemental analysis. As indicated by ^{1}H NMR *syn-syn*-**BBTB-OH** undergoes very slow degradation when stored in air, while *anti-anti* isomer is completely stable under ambient conditions.

In the second step, **BBTB-OH** were converted to B-chlorinated derivatives (**BBTB-Cl**), which were instantly reacted with freshly prepared phenyldipyrromethene precursor in the presence of a base {N(*i*-Pr)$_2$Et} to give corresponding BODIPY complexes (**BBTB-BODIPY**). Multinuclear NMR spectroscopy, X-ray crystallography, elemental analyses and HR-MS confirmed the structure and purity of the final products. Obtained complexes show long-term stability under ambient conditions both in solid state and solution.

Structural and physicochemical characterization of BBTB-OH. The molecular structures and selected crystal motifs of the two isomeric **BBTB-OH** are presented in **Figure 1**. The C–S bond lengths (1.72–1.74 Å) and C–S–C bond angles (101–103°) are comparable to the values found in the related **DBTB** structures.[78] The molecule of *anti-anti*-**BBTB-OH** is essentially planar, while the *syn-syn*-**BBTB-OH** is slightly bent with the angles between benzothiophene and [1,4]thiaborin mean planes of 4–6° (**Figure S4.1**, SI). In addition, the B–O bond deviates from the [1,4]thiaborin plane by 9°. Observed molecular distortions result from steric congestion provided by closely distanced O–H and C–H hydrogen atoms ($d_{H…H}$ = 1.93 Å < Σr_H^{vdW} = 2.2 Å). A through-space steric compression effect is reflected on the ^{1}H NMR spectra;[103,104] specifically, the signal ascribed to benzothieno H5/H13 protons is strongly upfield shifted ($\delta^{H5/H13}$ = 8.71 ppm), while the O–H proton downfield shifted (δ^{H1} = 9.56 ppm) compared to the corresponding signals on ^{1}H NMR spectrum of *anti-anti* isomer ($\delta^{H5/H13}$ = 8.12 ppm; δ^{H1} = 10.36 ppm). In accordance, the DFT calculations performed at the M062X/6-311++G(d,p) level of theory confirm higher stability of *anti-anti*-**BBTB-OH** (ΔG = 23.1 kJmol^{-1}).

The *anti-anti*-**BBTB-OH** isomer crystallizes with DMSO molecule connected to the B–OH hydroxyl group by a short O–H…O hydrogen bond ($d_{O…O}$ = 2.69(1) Å). A rigid and planar framework of **BBTB** facilitates formation of π-stacking interactions involving central [1,4]thiaborin ring bearing electropositive boron atom with electronegative oxygen, sulfur, or carbon atoms from the neighboring benzothiophene unit. Parallel molecules are oriented in a head-to-head fashion. In the case of *anti-anti*-**BBTB-OH**, the interactions between aromatic electron clouds are supported by more specific S…B interactions ($d_{S…B}$ = 3.50(1) Å). This leads to the significant horizontal displacement of the stacked molecules (**Figure S4.2**, SI). In contrast, the molecules in the crystal structure of *syn-syn*-**BBTB-OH** are vertically displaced due to the relatively weak B…O intermolecular interaction of 3.77(1) Å, sustaining head-to-head

fashion of molecular layout. Despite different mutual stacking arrangement, the dimer interaction energy calculated at M062X/6-311++G(d,p) level of theory is comparable for both isomers. The high interaction energy value of *ca.* −60 kJ·mol^{-1} indicates that dimers or other π-stacked aggregates may persist in concentrate solutions. Apart from the π-stacking interactions, the supramolecular structure of the *syn-syn* isomer is based on two other motifs involving O–H…O hydrogen and multiple S…S chalcogen bonds.

Topological analysis of electron density and its negative Laplacian function {$L(\mathbf{r}) = −\nabla^2\rho(\mathbf{r})$} within the quantum theory of atoms in molecules (QTAIM),[105] provides close insight into the mechanism of the formation of S…S chalcogen bond interactions. The molecular graph along with S…S BCPs, charge concentration (CC) and charge depletion (CD) points around sulfur atoms corresponding to the local maxima and minima of electron density, respectively, is shown in **Figure 1c**. Two charge concentration points appear in the plane bisecting the C–S–C angle. They can be directly associated with the lone electron pairs (LP) of the sulfur atoms. In addition to CC, two CD points located along the C–S bonds can be ascribed to the C–S antibonding orbitals, while the CD bisecting the C–S bonds agrees with the location of a σ-hole at the sulfur atom. The angular orientation of two neighboring molecules allows for optimal chalcogen interaction between sulfur atoms with lone electron pairs pointing toward charge depletion regions (σ-hole or σ*(C–S)). The values of electron density and Laplacian at BCPs (**Table S6.1**, SI) are comparable with experimental and theoretical values obtained for S…S interactions in thiophene-based systems.[106–108]
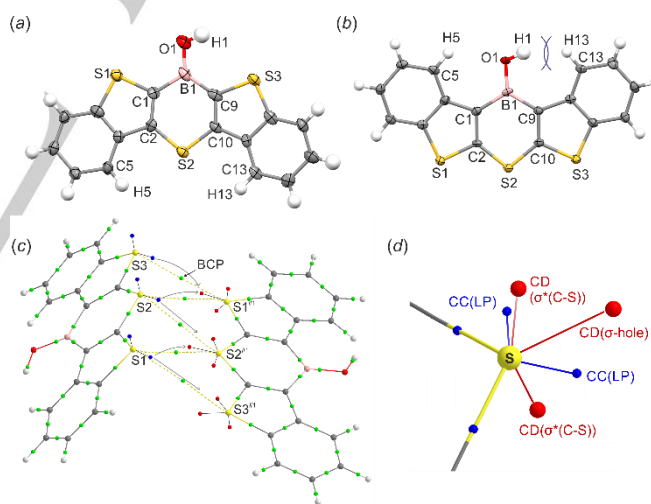

Figure 1. Molecular structures of (*a*) *anti-anti*-**BBTB-OH** and (*b*) *syn-syn*-**BBTB-OH**. Thermal ellipsoids were generated at 50% probability level. (*c*) Molecular graph showing S…S chalcogen bonds in *syn-syn*-**BBTB-OH** with the disposition of selected bond critical points {BCP(3, −1); green spheres}, charge concentration {CC(3, −3); blue spheres} and charge depletion points {CD(3, −1); red spheres}. Symmetry operation (#1): 1−*x*, −1/2+*y*, −*z*. (*d*) Laplacian's critical points around the sulfur atom (S2) in *syn-syn*-**BBTB-OH**.

The ^{11}B NMR spectra in DMSO-d_6 (**Figures S7.3** and **S7.6**, SI) show the appearance of two signals at 35 ppm and −6 ppm associated with three and tetracoordinate boron centers, respectively, indicating a strong Lewis acid character of **BBTB-OH** capable of coordination with solvent molecules (water or

DMSO). Lewis acidic character of studied compounds was further quantitatively evaluated from the calculation of the Gibbs free energy values for complexation of the OH^- and F^- anions (**Table S6.2**, SI). The lower Gibbs free energy values confirm stronger Lewis acidic character of ***syn-syn*-BBTB-OH**. This is also reflected by the higher Hirshfeld atomic charge at the boron atom {q(B) = 0.146 e} relative to the *anti-anti* isomer {q(B) = 0.126 e}. In addition, from the comparison of respective isomers of **BBTB-OH** and **DTTB-OH**, the former systems exhibit expected weaker Lewis acidity. This indicates that the extension of π-electron system by two side benzo units increases electron density at the boron atom leading eventually to larger total stabilization of the central [1,4]thiaborin unit.

The annulation mode also strongly affects the symmetry and energy of frontier molecular orbitals (**Figure S4.3**, SI). While HOMO energy of ***anti-anti*-BBTB-OH** (E_{HOMO} = −5.90 eV) is slightly elevated relative to the *syn-syn* isomer (E_{HOMO} = −6.05 eV), the LUMO energy is significantly decreased (E_{LUMO} = −2.04 eV for ***anti-anti*-BBTB-OH** and E_{LUMO} = −1.54 eV for ***syn-syn*-BBTB-OH**). The observed differences in electronic structures should be apparent in absorption and emission UV-Vis spectroscopy. As shown in UV-Vis spectra (**Figure 2**), the ***anti-anti*-BBTB-OH** exhibits two absorption maxima at 310 and 364 nm, and fluorescence at 378 nm (**Table S2.1**, SI). A rather distinct spectroscopic behavior is observed for the *syn-syn* isomer. Only one absorption band at λ_{abs} = 321 nm is observed, albeit, a new broad emission band at 588 nm appears. Furthermore, the intensities of emission bands are strongly concentration-dependent, both being quenched at c > 10^{-4} M (**Figure S2.12**, SI). This quenching effect can be ascribed to the formation of π-stacked aggregates.

Calculated absorption and emission wavelengths generally correspond to the observed experimental bands, however, the calculations do not reproduce the red emission band in the *syn-syn* isomer. We suppose that it corresponds to some dimeric or oligomeric structures formed due to chemical transformation under light irradiation. We have noted that the intensity of this band slowly increases over several days. This is accompanied by the turning of the initial colourless solution into pink. The ^{1}H NMR analysis indicates the appearance of additional signals in the
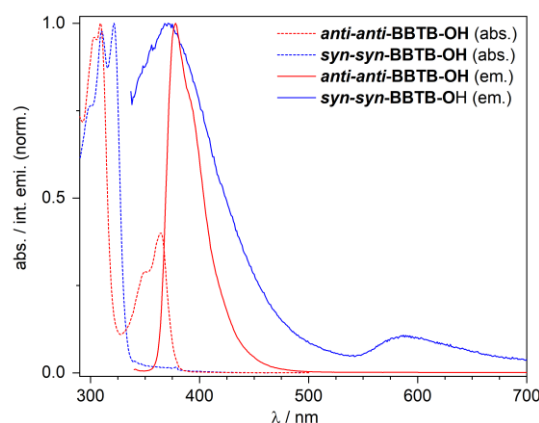

Figure 2. Absorption and emission spectra of **BBTB-OH** in toluene solution.

aromatic region (**Figure S7.7**, SI). Notably, such effects were not observed for the *anti-anti* isomer, which agrees with its generally higher stability.

To obtain further insight into the aromatic character of the studied thiaboracycles, we have carried out nucleus-independent chemical shift (NICS) calculations using GIAO protocol with B3LYP/6-311++G(g,p) level of theory. NICS were derived from calculations of the isotropic magnetic shielding (taken with a negative value) at the centroid of the aromatic rings {NICS(0)} and 1 Å above and below the centroid (NICS(1) – taken as an average value). Benzene, thiophene, and 4-hydroxy-[1,4]thiaborin were used as reference systems. According to our results, the NICS(0) and NICS(1) values for 4-hydroxy[1,4]thiaborin are −3.36 ppm and −4.64 ppm, respectively, suggesting their moderate aromatic character. The fusion of thienyl rings leads to the weakening of aromaticity in **DDTB-OH**, which is even further reduced upon extension with peripheral benzene rings in **BBTB-OH** (**Table 1**). At the same time, the aromatic character of thienyl rings is significantly lower with respect to thiophene, while NICS values for the side benzo rings are comparable to benzene. Importantly, the aromaticity of the central [1,4]thiaborin and thienyl rings is considerably lower for the *syn-syn* isomer compared to

Table 1. Comparison of NICS(0) and NICS(1) aromatic indicators in **BBTB-OH**, **DTTB-OH**, and referential compounds. All NICS values are provided in ppm.

Compound	[1,4]thiaborin		thienyl		benzo	
	NICS(0)	NICS(1)	NICS(0)	NICS(1)	NICS(0)	NICS(1)
4-hydroxy-[1,4]thiaborin	−3.36	−4.64	-	-	-	-
thiophene	-	-	−12.93	−10.28	-	-
benzene	-	-	-	-	−8.06	−10.23
***anti-anti*-DTTB-OH**[a]	−3.50	−3.95	−11.37	−9.41	-	-
***syn-syn*-DTTB-OH**[a]	−2.85	−3.51	−10.50	−8.86	-	-
***anti-anti*-BBTB-OH**[a]	−3.18	−3.83	−9.10	−8.08	−8.82	−10.31
***syn-syn*-BBTB-OH**[a]	−2.72	−3.31	−8.21	−7.39	−9.08	−10.49

[a] NICS(0)/NICS(1) values are similar for two thiophene and benzene rings and therefore they were taken as average values.

the *anti-anti* counterpart. This is partially counterbalanced by the enhanced aromaticity of the peripheral benzene rings. Thus, it can be concluded that delocalization of the π-electron density is more efficient for ***anti-anti*-BBTB-OH**. This correlates with its lower boron Lewis acidity, higher stability, and red-shifted absorption and emission bands.

Structural and optical properties of BBTB-BODIPY complexes. The single crystals of **BBTB-BODIPY** were obtained by diffusion method in DCM/hexane binary solvent system. Molecular structures are presented in **Figure 4**. In addition, we have obtained two toluene solvatomorphs of ***syn-syn*-BBTB-BODIPY**, namely ***syn-syn*-BBTB-BODIPY·PhMe-A** and ***syn-syn*-BBTB-BODIPY·PhMe-B**. They crystallize in orthorhombic ($Pca2_1$) and monoclinic ($P2_1/c$) crystal systems, respectively, both with one toluene and one **BBTB-BODIPY** molecule in the asymmetric part of the unit cell. Solvatomorphs are in polymorphic structural relation. All structures reveal the perpendicular *spiro* arrangement of the BBTB and BODIPY moieties around the central boron node. The molecular geometries of all ***syn-syn*-BBTB-BODIPY** crystal forms are very similar (**Figure S4.5**, **Table S4.3**, SI) indicating that they are not significantly affected by the crystal field. The observed conformational rigidity results from the close proximity of the BODIPY unit and the peripheral BBTB-benzo units, and indicating that likely the molecule remains rigid in solution. In contrast, in ***anti-anti*-BBTB-BODIPY** the internal strains are partially alleviated leading to a more pronounced conformational lability. As indicated by the $\alpha_{C21-B1-S2}$ angle of 165.8(1)° the BBTB mean plane is in-plane shifted with respect to the ligand (**Figure 3a**). The *meso*-Ph group is even further shifted with $\alpha_{C30-C21-B1}$ angle value of 168.8(1)°. Apart from the in-plane distortions, the BBTB and BODIPY mean planes deviate from their mutual perpendicular arrangement, which is manifested by their rudder-like out-of-plane displacement (**Figure 3a**). DFT optimization of the ***anti-anti*-BBTB-BODIPY** molecule restores its ideal perpendicular conformation (**Figure S6.8**, SI). The energy difference between experimental (hydrogen atoms optimized while positions of other atoms preserved) and fully optimized theoretical structures is 11 kJ·mol^{-1}. This leads to the conclusion that the observed molecular distortions result from the crystal field effects, while some conformational mobility can be expected in solution. We suppose that molecular mobility may influence optical properties of the system,[109,110] as different conformers may excite to energetically different states resulting in distinct intersystem crossing rates.

Orthogonal *spiro* arrangement of BBTB and BODIPY moieties prevents close π-stacking interactions between flat molecular components as observed in **BBTB-OH**. Instead, the supramolecular structures are dominated by C−H…C(π) interactions forming slipped molecular stacks referred to as *J*-aggregates (**Figure 3**). The distances between boron centers in such motifs are 8.124 Å (*anti-anti* isomer) and 7.887 Å (*syn-syn* isomer), while the interplane distances between the dipyrromethene moieties are 3.568 Å (*anti-anti* isomer) and 3.463 Å (*syn-syn* isomer) resulting in slip angle of 26° for both isomers. The formation of *J*-aggregates is also observed in both toluene solvatomorphic forms of ***syn-syn*-BBTB-BODIPY** (**Figure S4.4**, SI). The distances between boron centers (7.633 Å and 7.675 Å), dipyrromethene interplane distances (3.443 Å and 3.547 Å), and slip angles (27° and 28°) are comparable with the non-solvated structure. However, the neighboring molecules are positioned differently, adapting either a head-to-head or head-to-tail

orientation. Computations show that dimer interaction energies are high for *J*-aggregates ranging from −44.9 kJ·mol^{-1} to −59.3 kJ·mol^{-1}, remaining the strongest among other dimers in the corresponding crystal structures (**Table S6.3**, SI). This indicates that different types of *J*-aggregates may persist in concentrated solutions and thin films, further affecting their spectral properties.

Both complexes display reversible first oxidation and first reduction cycles evident in the cyclic voltammograms (**Figure S5.1**, SI). Despite the differences in electronic properties of the parent **BBTB-OH** systems, oxidation half-wave potentials are comparable between the two isomeric **BBTB-BODIPY** (**Table 2**) counterparts. In turn, for ***anti-anti*-BBTB-BODIPY** the reduction half-wave potential is elevated by 0.10 V with respect to ***syn-syn*-BBTB-BODIPY**. The obtained redox potentials are generally in agreement with the values obtained for *spiro*
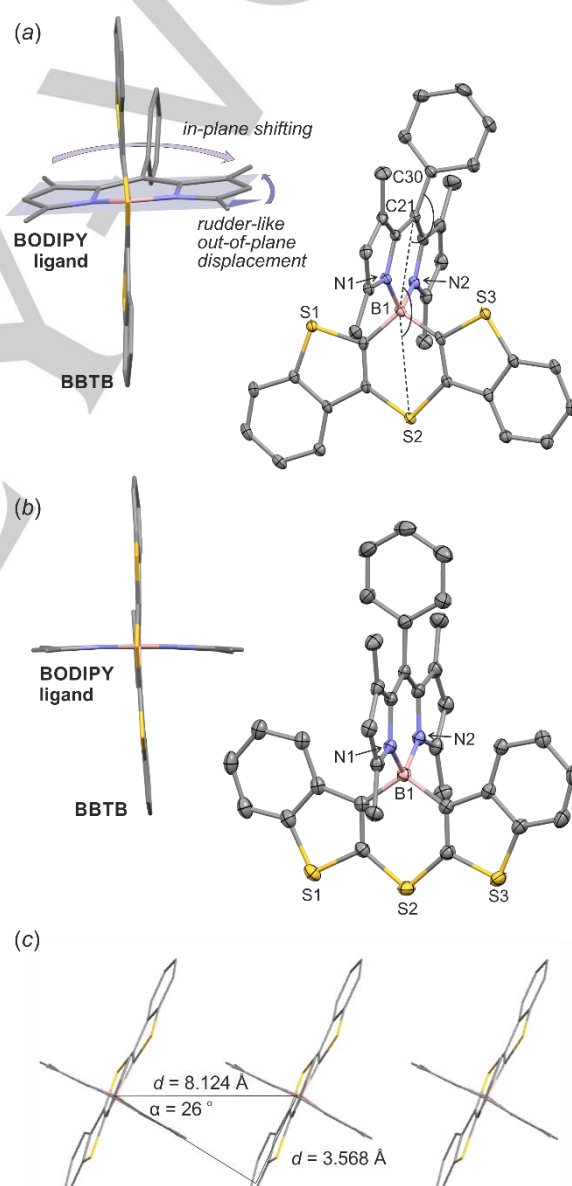

Figure 3. Molecular structures of (*a*) ***anti-anti*-BBTB-BODIPY** and (*b*) ***syn-syn*-BBTB-BODIPY**. Fragment of crystal structure of (*c*) ***anti-anti*-BBTB-BODIPY** presenting the formation of *J*-aggregates. Thermal ellipsoids were generated at 50% probability level. Hydrogen atoms are omitted for clarity.

Table 2. Summary of electrochemical redox potentials recorded in 0.1 M n-Bu$_4$NBF$_4$/CH$_2$Cl$_2$ for **BBTB-BODIPY** with cyclic voltammetry at a scan rate of 50 mV s^{-1}.

Compound	E_{onset}^{ox} [a]/ V	E_{onset}^{red} [b]/ V	IP[c] / eV	EA[d] / eV	$E_{1/2}^{ox}$ [e] / V	$E_{1/2}^{red}$ [f] / V
***anti-anti*-BBTB-BODIPY**	0.53	−1.77	5.63	3.33	0.63	−1.84
***syn-syn*-BBTB-BODIPY**	0.56	−1.88	5.66	3.22	0.65	−1.94

[a] Oxidation onset potential, V; [b] Reduction onset potential, V; [c] Ionization potential, IP = e[E_{onset}^{ox}] + 5.1, eV; [d] Electron affinity, IP = e[E_{onset}^{red}] + 5.1, eV. [e] Oxidation half-wave potential; [f] Reduction half-wave potential.

borafluorene-BODIPY dyads studied by Wang.[111] In parallel, the DFT (B3LYP/6-311++G(d,p) level of theory) calculations show that the HOMO is located solely on the BBTB core, while LUMO resides on the BODIPY moiety (**Figures S6.6** and **S6.7**, SI). This indicates that BBTB will act as an electron donor and BODIPY as an electron acceptor in the electron transfer process.

The optical properties of **BBTB-BODIPY** dyes were investigated in 5 solvents with different polarity including cyclohexane (chex), toluene (PhMe), chloroform (CHCl$_3$), acetonitrile (MeCN), and ethanol (EtOH). Regardless of the choice of solvent, both complexes exhibit a vibronically resolved absorption band at 495–505 nm, showing a very similar absorption profile to other BODIPY complexes.[112] The emission spectra reveal presence of two luminescent components (**Figure 4**, **Table 3**). The dominant component at 510–525 nm is only slightly dependent on solvent polarity, *i.e.* only a slight negative solvatochromic shift is observed. We attribute this component to emission from singlet local excited state (^{1}LE) of the BODIPY unit, with excited state lifetimes in the range of 1.5–4.9 ns.[112] As a consequence of a more rigid structure, the absorption and photoluminescence maxima for the *syn-syn* isomer are systematically blue-shifted by 220–260 cm^{-1} with respect to the

anti-anti isomer. Along with the ^{1}LE emission band, a broad band at 550–800 nm can be observed. Emission lifetimes of this luminescent component are in the range of 0.69–4.15 ns indicating a fluorescent character of this transition. This photoluminescent component displays evident positive solvatochromic shifts for both isomers. Thus, we believe this band likely originates from a singlet charge-transfer excited state (^{1}CT). The position and intensity of the ^{1}CT band are strongly affected by the annulation mode reflecting the differences in the electronic structures of both BBTB scaffolds. Specifically, the ^{1}CT band in the *anti-anti* derivative is red-shifted by 700–1200 cm^{-1} with respect to its counterpart. This can be associated with enhanced π-conjugation in the *anti-anti*-BBTB core, providing higher stabilization of the ^{1}CT state. This is further confirmed by theoretical calculations discussed in the latter part of the article.

Unlike typical BODIPY complexes that are generally highly luminescent in dilute solutions,[113] **BBTB-BODIPY** fluorescence is almost completely quenched (QY^F < 3 %). Low temperature (T = 77 K) time-resolved photoluminescence spectra recorded in

Table 3. UV-Vis absorption and emission data for **BBTB-BODIPY** complexes in different solvents, solid state, and Zeonex film together with fluorescence lifetimes recorded with TCSPC. QY^F stands for fluorescent quantum yields, $\Delta\tilde{v}$ for Stokes shifts, and τ for fluorescent lifetimes. ^{1}LE and ^{1}CT refer to local and charge transfer excited states, respectively.

	Solvent (ε)[a]	λ_{abs} / nm (ε[b] / 10^4 M^{-1} cm^{-1})	λ_{em}(^{1}LE)[c] / nm	$\Delta\tilde{v}$ / cm^{-1}	τ_{LE} / ns	λ_{em}(^{1}CT)[c] / nm	τ_{CT} / ns	QY^F / %
***anti-anti*-BBTB-BODIPY**	chex (2.02)	504	522	680	1.89(9) / 3.7(2)[d]	602	0.69(1) / 3.97(3)[d]	0.5%
	PhMe (2.38)	506 (9.42)	523	640	2.38(2)	604	0.88(2) / 3.8(1)[d]	0.2%
	CHCl$_3$ (4.81)	504 (7.18)	520	610	2.84(5)	642	0.79(2) / 4.15(6)[d]	0.2%
	MeCN (37.5)	499	516	660	1.69(3) / 4.0(1)[d]	649	-	0.2%
	EtOH (24.5)	501	518	655	2.86(1)	641	3.52(1)	0.7%
***syn-syn*-BBTB-BODIPY**	chex (2.02)	501	515	540	2.56(1)	574	2.69 (1)	2.8%
	PhMe (2.38)	502 (7.53)	516	540	2.55(1)	595	2.51(1)	1.1%
	CHCl$_3$ (4.81)	501 (6.59)	514	505	2.64(1)	597	2.38(1)	0.6%
	MeCN (37.5)	496	509	515	2.45(8) / 4.9(1)[d]	621	2.43(1)	0.3%
	EtOH (24.5)	498	512	550	3.45(1)	610	2.58(1)	0.9%

[a] Solvent dielectric constant is provided in brackets. [b] Molar absorption coefficient can only be reliably evaluated in PhMe and CHCl$_3$ solutions, in the remaining solvents the solubility is too low. [c] The values were estimated by deconvoluting experimental spectra. [d]Fluorescence lifetimes obtained from a bi-exponential fit of the TCSPC traces.
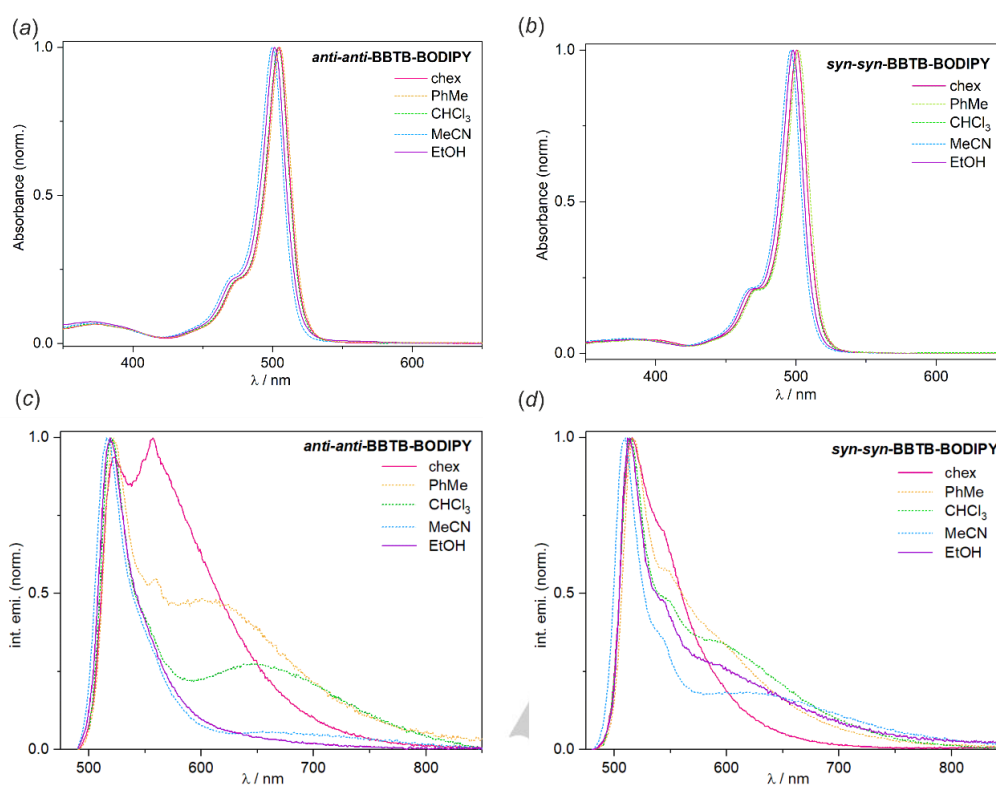
Figure 4. (*a*, *b*) Absorption and (*c*, *d*) emission spectra of **BBTB-BODIPYs** in various solvents.

0.5 % Zeonex thin films show intense near infrared phosphorescence band at λ_{em} = 732 nm for ***anti-anti*-BBTB-BODIPY** and λ_{em} = 727 nm for ***syn-syn*-BBTB-BODIPY** (**Figure 5**). The phosphorescence spectra display a second vibronic peak at *ca*. 820 nm with potentially other vibronic peaks extending out beyond the spectral window. Phosphorescence lifetimes were estimated at ~200 ms. Such relatively long phosphorescence lifetime is suggestive of its dominating π-π* ^{3}LE character. Strongly phosphorescent properties of both **BBTB-BODIPY** isomeric complexes are indicative of fast intersystem crossing and elevated triplet formation yields in optical excitation, which is consistent with the unusually low fluorescence quantum yields.

Emission spectra of both **BBTB-BODIPY** isomers in powder are drastically different from the spectra in solution. In particular, the emission band at 520 nm, observed in solution, is not present, which is accompanied by the appearance of a red-shifted broad emission band with maximum at 672 nm in ***anti-anti*-BBTB-BODIPY** and 637 nm in ***syn-syn*-BBTB-BODIPY** (**Table 4**, **Figure 6**). Both of the emission spectra display broad photoluminescence shoulders at λ > 700 nm. These differences can be attributed to *J*-aggregate formation as usually observed in other dyes displaying *J*-aggregate crystal motifs.[111,114–116] It should be noted that the fluorescence quantum yield of ***anti-anti*-BBTB-BODIPY** in solid state is higher by a factor of 15 with respect to dilute solution, suggesting aggregation-induced emission (AIE) behavior of this luminophore.[111,117] Despite this increase however the QY^F remains relatively low. To further study the AIE behavior of the two luminophores we record fluorescence intensity in MeCN/water mixtures with different volumetric fractions of water. The experiment shows that a fluorescence

band at 633 nm in ***anti-anti*-BBTB-BODIPY** emerges and then significantly increases when water content exceeds 60 % (**Figure S2.1**, SI). This behavior is consistent with *J*-aggregate formation.

To further investigate the optical properties of the **BBTB-BODIPY** dyes, we have prepared Zeonex[118] thin films with concentrations ranging from 0.005 %$_{wt}$ to 10 %$_{wt}$ (**Figure 6**). The emission spectra in low concentration films at room temperature are generally similar to those recorded in cyclohexane solution, consistent with the low polarity environment of the Zeonex host.
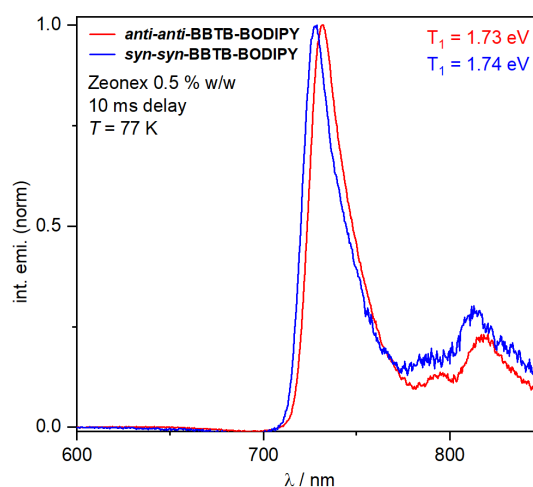

Figure 5. Phosphorescence spectra of **BBTB-BODIPY** isomers recorded in 0.5% Zeonex thin films at 77 K.
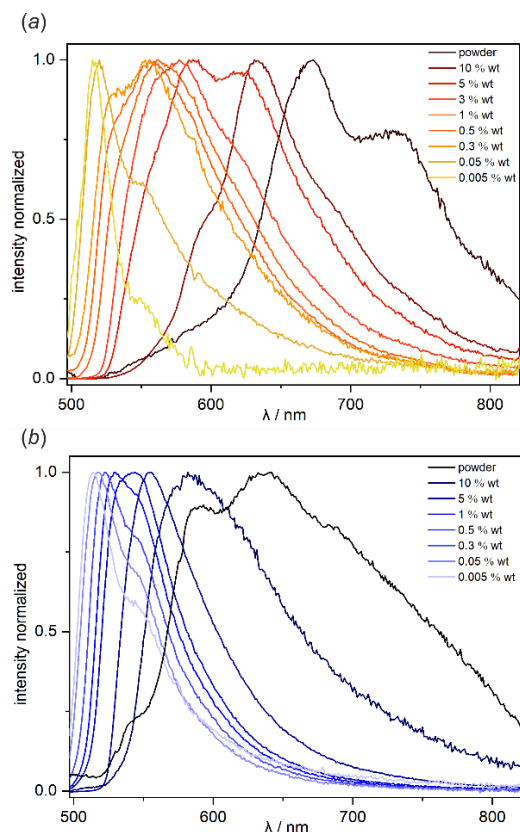
Figure 6. Emission spectra in Zeonex films at gradually increasing weight concentrations for (*a*) *anti-anti*-**BBTB**-**BODIPY** and (*b*) *syn-syn*-**BBTB**-**BODIPY**. Respective photoluminescence spectra recorded in powder are shown for comparison.

Table 4. Summary of photoluminescence properties of **BBTB-BODIPY** complexes in powder and Zeonex films.

		λ_{em} / nm	QY^F / %
anti-anti-**BBTB**-**BODIPY**	Zeonex (0.005 %)	515	0.1%
	Zeonex (10 %)	632	0.1%
	Powder	672, 732	6.5%
syn-syn-**BBTB**-**BODIPY**	Zeonex (0.005 %)	513	3.7%
	Zeonex (10 %)	582	5.9%
	Powder	590, 637, 684	1.3%

When the concentration reaches 10 %, the emission spectra become more similar to the spectra in powder. Interestingly, fluorescence spectra recorded at intermediate concentrations are not a simple sum of the luminescent components recorded in 0.005 %wt and at 10 %wt films. Instead, both complexes exhibit a systematic bathochromic shift of the emission spectrum with increasing dye concentration. This suggests a gradually increasing size of the aggregates formed. Consistent with this finding is a further red shifted photoluminescence in bulk powder.

Photocatalytic activity of BBTB-BODIPY. The observed formation of long-lived ^{3}LE triplet states suggests the possibility of using **BBTB-BODIPY** as singlet oxygen photosensitizers. The efficiency of this process was determined by monitoring the drop in intensity the absorption band of 1,3-diphenylisobenzofuran (DPBF, λ_{abs} = 412 nm) - a well-known chemical trap for $^1O_2$ detection (**Figure S3.5**, SI). According to our results, **BBTB-BODIPY** complexes show quantum high yields of singlet oxygen production (QY^O) in DCM of 73 % and 77 % for the *anti-anti* and *syn-syn* isomers, respectively. These values are comparable to that of 2,6-diiodinated BF$_2$-BODIPY (QY^O = 79 %, MeCN),[119] Rose Bengal (RB; QY^O = 79 %, MeOH)[120] or 5,10,15,20-tetraphenylporphyrin (TPP; QY^O = 55 %, CHCl$_3$).[121]

To further verify the usability of **BBTB-BODIPY** complexes as singlet oxygen photosensitizers, we have performed a series of oxidation reactions using 2-furoic acid as a model organic reagent. The oxidation of 2-furoic acid with singlet oxygen proceeds according to the [2+4] cycloaddition mechanism leading to 5-hydroxyfuranone as the final oxidation product. Samples containing 0.05 %$_{mol}$ photosensitizer with respect to the starting compound were dissolved in CHCl$_3$ and irradiated with neutral-white LED light under air at 25 °C (irradiance: 1200 W·m^{-2}). Progress of the reaction was monitored using ^{1}H NMR. In parallel experiments, stability of the photosensitizers were tested maintaining conditions from photocatalytic reactions with 2-furoic acid (**Figures S3.1**-**S3.3**, SI). Both complexes demonstrate high photostability with the estimated half-life of *ca.* 60 h for *anti-anti*-**BBTB**-**BODIPY** and *ca.* 200 h for *syn-syn*-**BBTB**-**BODIPY**. For comparison, widely studied Rose Bengal (RB) and 5,10,15,20-tetraphenylporphyrin (TPP) photocatalysts half-decompose after 0.5 h and 16 h of irradiation, respectively (measured at the same conditions).[80] In addition, both **BBTB-BODIPY** complexes are resistant toward hydrolysis, which can be concluded from stability experiments performed at the same conditions, but without irradiation (**Figures S3.1** and **S3.2**, SI).

Photocatalytic experiments clearly show that **BBTB**-**BODIPY** catalysts are very active singlet oxygen generators with the total conversion of 2-furoic acid achieved after 1.5 h (turnover frequency, TOF = 1330 h^{-1}) and 2 h (TOF = 1000 h^{-1}) for the *anti-anti* and *syn-syn* isomers, respectively (**Figure 7**). They outperform RB (TOF = 494 h^{-1}) and TPP (TOF = 446 h^{-1}) photocatalysts, studied in the same conditions.[80] We have
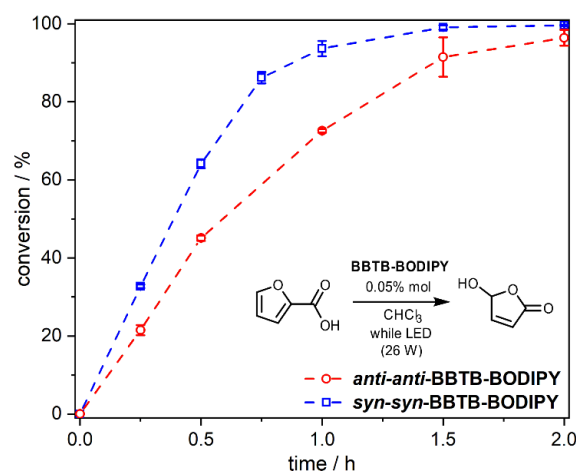

Figure 7. Reaction profiles for the catalytic oxidation of 2-furoic acid with 0.05 % **BBTB**-**BODIPY**. Conditions: T = 25 °C; constant stirring and irradiation, 26 W neutral-white LED source; sample irradiance: 1200 W·m^{-2}; 2-furoic acid concentration c = 12 mg·mL^{-1}.

observed that the *syn-syn* isomer is more active which is in agreement with its higher QY[O] value. Enhanced activity of ***syn-syn*-BBTB-BODIPY** probably results from its lower conformational lability. We speculate that some mutual movements between BBTB and BODIPY units activate deexcitation pathways from the triplet state, although further studies are necessary to confirm this hypothesis.

DFT computations. To shed more light on the mechanism underpinning the observed photocatalytic activity of **BBTB-BODIPY** complexes we have performed a series of TD-DFT calculations at B3LYP/6-311++G(d,p) level of theory. The character of the excited states was deduced from natural transition orbitals analysis (NTOs). We predict two main absorption maxima at *ca.* 450 nm and 600 nm. The absorption at 450 nm can be associated with the experimentally observed band, although it is typically underestimated with respect to the experimental value (~500 nm). The longer-wavelength absorption band involves a transition between HOMO and LUMO orbitals localized on the BBTB and BODIPY units, respectively. It can be thus ascribed to a charge transfer transition, which, due to the perpendicular orientation of both moieties, is almost forbidden and therefore displays a negligible absorption coefficient.

The TD-DFT calculations reveal the two lowest singlet excited states with a CT character ($^1CT_1$ and $^1CT_2$), a third singlet excited state displaying hybrid local-charge transfer character ($^1HLCT_3$) and a fourth BODIPY-localized state ($^1LE_4$). Furthermore, we also find two low-energy triplet states: $^3LE_1$ localized on the BODIPY moiety and $^3CT_2$ of a charge-transfer nature. The localized character of the $^3LE_1$ is also confirmed by the spin density calculation (**Figure S6.14**, SI). The energy of this state is 1.46 eV for the *anti-anti* and 1.47 eV for the *syn-syn* isomers, respectively, and is comparable to the triplet energy found in compact donor-acceptor BODIPY photosensitizers.[81,83,122–130] We believe the observed fluorescence emission at *ca.* 520 nm originates from the $^1HLCT_3$ or $^1LE_4$ states, while the more red-shifted emission in solutions can be attributed the $^1CT_1$ or $^1CT_2$ states. The assignment of $^3LE_1$ character to the lowest triplet state agrees with the experimental data. This is evidenced by a resolved structure of the phosphorescence spectrum with two clear maxima visible in the spectral window: at *ca.* 730 nm and 820 nm. Populating the $^1CT_1$ state most likely occurs via the electron transfer from the BBTB to the BODIPY moieties (process **2**, **Figure 8**). In a subsequent step $^1CT_1$ state converts to higher vibronic levels of $^3LE_1$ state *via* spin-orbit charge transfer

intersystem crossing (SOCT-ISC, process **3b**). The SOCT-ISC mechanism has been postulated for related borafluorene-based BODIPY photosensitizers,[80] as well as other compact donor-acceptor BODIPY dyads[81,128–139] and is broadly recognized as the important underlying mechanism for ISC and reverse ISC (RISC) in thermally activated delayed fluorescence (TADF) emitters.[140]

Conclusion

We have developed a synthetic route to bis[1]benzothieno[1,4]thiaborins – new boracyclic scaffolds composed of a central [1,4]thiaborin ring fused with two benzothiophene aromatic units. scXRD analysis shows that the obtained **BBTB-OH** are characterized by planar molecular structures, although some deviation from planar geometry is observed due to internal strains in the case of the *syn-syn* isomer. DFT calculations show that ***anti-anti*-BBTB-OH** is characterized by a more advantageous π-conjugation leading to an increased aromatic character of the central [1,4]thiaborin ring and larger stabilization of the LUMO energy level. The observed differences in electronic structures are reflected in their optical properties, *i.e.* absorption and emission bands of the *anti-anti* isomer are bathochromically shifted with respect to the *syn-syn* isomer.

The **BBTB-OH** boracycles were converted to respective **BBTB-BODIPY** complexes. Although both complexes share some similar photophysical features resulting from the same ligand structure, important differences are visible in the red region of the emission spectra. This is especially noticeable in the positions and intensities of the ^1CT emission bands as well as in solid-state luminescence behavior reflected in strong *J*-aggregation-induced red-shifted emission for both isomers and AIE behavior of the *anti-anti* isomer. The photophysical analysis and TD-DFT calculations revealed that **BBTB** can serve as a donor in the formation of a ^1CT state. The intense near infrared phosphorescence observed at low temperature in Zeonex films and very weak fluorescence intensity indicate efficient intersystem crossing leading to elevated triplet formation yields. Both complexes can serve as very effective photocatalysts with full conversions achieved within 2 h with only 0.05 %[mol] catalyst load, as evidenced by oxidation of 2-furoic acid with the photogenerated $^1O_2$.
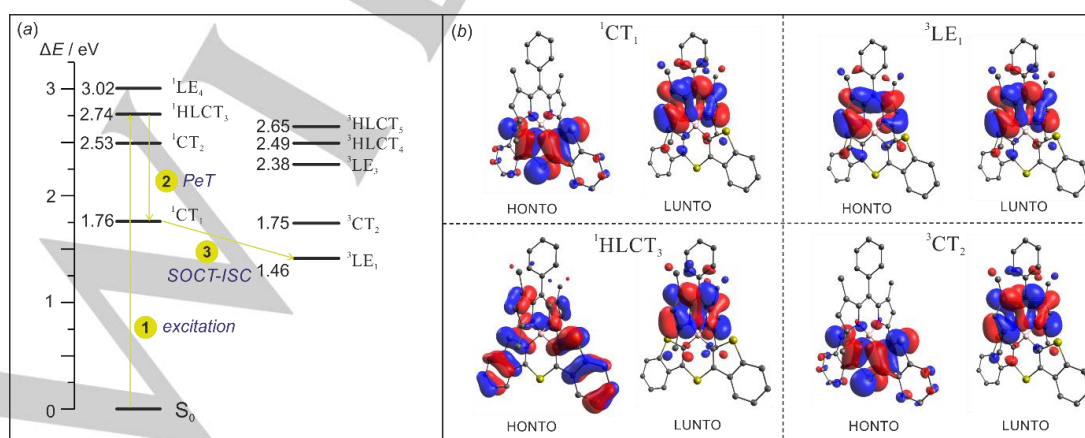

Figure 8. (*a*) Calculated energy diagram demonstrating the photophysical processes in ***anti-anti*-BBTB-BODIPY** (analogous energy diagram was obtained for *syn-syn* isomer presented in **Figure S6.5** in SI). (*b*) NTOs for singlet and triplet excited states relevant to the formation of the lowest-energy triplet excited state.

9

Experimental Section

Optical properties: The UV-Vis absorption spectra were recorded using a Hitachi UV-2300II spectrometer. The emission spectra of solutions were recorded using Edinburgh FS5 equipped with an enhanced range photomultiplier detector (PMT-EXT). The measurements were performed at room temperature, according to published procedures.[141,142] Suprasil quartz cuvettes (10.00 mm) were used. 1.5 nm slits were used for absorption and emission spectra. To eliminate any background emission, the spectrum of pure solvent was subtracted from the samples' spectra. Quantum yields of emission were determined in diluted solutions (OD < 0.03 for longest wavelength band) by comparison with known standards – **BBTB-OH**: Quinine sulfate (0.05 M H_2SO_4 solution, QY^F = 0.5244),[143] **BBTB-BODIPY**: fluorescein (0.1 M NaOH, QY^F = 0.92).[144] Concentrations of **BBTB-OH** and **BBTB-BODIPY** were adjusted to reach similar absorbance to the absorbance of reference solution at the excitation wavelength. Both compounds were excited at 380 nm. Fluorescence quantum yield was calculated according to the formula (1).

$$QY_x^F = QY_r^F \cdot \frac{F_x}{F_{st}} \cdot \frac{1 - 10^{-A_{st}}}{1 - 10^{-A_x}} \cdot \frac{n_x^2}{n_{st}^2} \tag{1}$$

Where F is the integrated photon flux (2) of sample (x) and reference (r), A is the absorbance at the excitation wavelength, n is the refractive index of used solvents.

$$F = \int I_c \, d\lambda_{em} = \int \frac{I(\lambda_{em})}{s(\lambda_{em})} d\lambda_{em} \tag{2}$$

Photon fluxes (F) were calculated by integration of corrected spectra (I_c), obtained by (I) division of intensity of emission spectra by the spectral responsivity (s) in corresponding wavelengths (λ_{em}). All measurements were carried out at room temperature.

Emission spectra of powder samples and thin Zeonex films were measured using front-face collection mode. Quantum yields of powder samples and thin Zeonex films were measured using an integrating sphere (Edinburgh Instruments FS5) according to the known procedure.[145] Solid samples were excited at the wavelength corresponding to the absorption maximum observed in the solid state. Thin Zeonex films were obtained *via* drop casting on quartz substrates. Chloroform solutions (mass ratio from 0.005 to 10 %) were deposited on quartz plates, let to dry, and vacuum-dried.

Fluorescence lifetime measurements were acquired using Time Correlated Single Photon Counting (TCSPC) system equipped with a picosecond pulsed 340 nm EPLED source.

Phosphorescence lifetime and spectra were recorded using nanosecond gated luminescence and lifetime measurements (from 400 ps to 1 s) with the third harmonic of a high-energy pulsed Nd:YAG laser emitting at 355 nm (EKSPLA) as the excitation source. The emitted light was focused onto a spectrograph and detected with a sensitive gated iCCD camera (Stanford Computer Optics) having sub-nanosecond resolution. Further details are available in reference.[146] Cryogenic conditions in this experiment were obtained using a liquid nitrogen cryostat VNF-100 (sample in flowing vapor, Janis Research).

Theoretical calculations: (1) Methods: Theoretical calculations were performed using *Gaussian16* program.[147] Molecules were optimized using M062X (DFT)[148] method with 6-311++G(d,p) basis set.[149] Molecular orbitals and TD-DFT calculations were performed using B3LYP functional[149,150] at the 6-311++G(d,p) basis set. **(2) Optimization:** The starting geometries were adopted from corresponding crystal structures. Prior to optimization, C-H bonds were elongated to standard neutron values. Following geometry optimization, the vibrational frequencies were calculated and the results showed that optimized structures are stable geometric structures. In optimization processes no symmetry constraints were applied. **(3) Intermolecular interaction energies:** The dimer interaction energies were calculated using the supermolecular method including Basis Set Superposition Error (BSSE). The dimers were extracted from the crystal structure and all C–H bonds were elongated to

average neutron values. **(4) Acidic properties:** The Lewis acidic properties of **BBTB-OH** were evaluated from the calculations of Gibbs free energy for the complexation of hydroxyl group or fluoride ion to respective boron centers. All calculations were performed using solvent field of water. **(5) QTAIM:** The topological analyses of the calculated electron densities were accomplished in terms of the QTAIM approach[105] and were carried out using *AIMAll*.[151] In the framework of this approach critical points (CPs) together with the bond paths (BPs) were found as well as charge concentrations (CC) and charge depletion (CD) points. To determine the nature and relative strength of intermolecular interactions, electron density, and its Laplacian was evaluated at the BCPs. **(6) NICS:** Nucleus-independent chemical shifts (NICS) were calculated for points located at the center of the aromatic rings (NICS(0)) and the points 1Å above and below the center of the ring.[152] The latter values were averaged to yield NICS(1). NICS is defined as the negative value of the absolute shielding computed at a certain point. The computations were performed applying GIAO procedure in *Gaussian16*. **(7) TD-DFT calculations:** Excited state geometries of **BBTB-BODIPY** were obtained with TD-DFT methods starting from ground state optimized geometries. To take into account the conditions of fluorescence measurements, TD-DFT calculations were carried out in the presence of the DCM solvent field with the polarizable continuum model (PCM) using the CPCM polarizable conductor calculation model.[153] Obtained singlet and triplet excited state geometries are quite similar and overlap with corresponding ground state geometries. For each excited state, natural transition orbitals (NTO) were calculated.[154] The MOs and NTOs were visualized with the *Avogadro*.[155]

Electrochemistry: Cyclic voltammetry was conducted in a three-electrode, one-compartment cell. All measurements were performed using 0.1 M Bu_4NBF_4 (99%, Sigma Aldrich, dried) solution in dichloromethane (ExtraDry AcroSeal®, Acros Organics). All solutions were bubbled with nitrogen prior to measurement and the measurement was conducted in nitrogen atmosphere. Electrodes: working (Pt disc d = 1 mm), counter (Pt wire), reference (Ag/AgCl calibrated against ferrocene). All cyclic voltammetry measurements were performed at room temperature with a scan rate of 50 mV s^{-1}. The ionization potential (IP) and electron affinity (EA) are obtained from onset redox potentials; these figures correspond to HOMO and LUMO values, respectively. The ionization potential is calculated from onset oxidation potential IP = e[E_{onset}^{OX}] + 5.1 eV and the electron affinity is calculated from onset reduction potential EA = e[E_{onset}^{RED}] + 5.1 eV.[156–159] We assume an uncertainty of ±0.02 V to the determined redox potentials.

X-ray crystallography: Single crystals of **BBTB-OH** and **BBTB-BODIPY** were obtained by slow evaporation of DMSO, CHCl₃ or toluene solutions. All crystals were measured at 100 K on SuperNova diffractometer equipped with Atlas detector (Cu-K_α radiation, λ = 1.54184 Å or Mo-K_α radiation, λ = 0.71073 Å). In all cases a selected crystal was maintained at a low temperature (T = 100 K) with the use of Oxford Cryosystems nitrogen gas-flow device. The crystal structures were established conventionally *via* X-ray data refinement employing the Independent Atom Model (IAM). Data reduction and analysis were carried out with the *CrysAlisPro* suites of programs.[160] All structures were solved by intrinsic phasing using *SHELXT*[161] and refined using *SHELXL-2014*[162] with *Olex2* suite.[163] All non-hydrogen atoms were refined anisotropically. All carbon-bound hydrogen atoms were placed in calculated positions with the C–H distances of 0.95 Å and U_{iso}(H) = 1.2U_{eq}(C). The positions of O–H hydrogen atoms in **BBTB-OH** were derived from difference electron density maps, then the O–H distances were fixed to 0.84 Å with a standard deviation of 0.01 Å. All-important crystallographic data including measurement, reduction, structure solution, and refinement details are included in **Tables S4.1** and **S4.2**. (SI) or in the associated CIF files. Deposition Number(s) <url href="https://www.ccdc.cam.ac.uk/services/structures?id=doi:10.1002/chem.202300680"> 2209296 (for *anti-anti*-**BBTB-OH**), 2209297 (for *syn-syn*-**BBTB-OH**), 2209298 (for *anti-anti*-**BBTB-BODIPY**), 2209299 (for *syn-syn*-**BBTB-BODIPY**), 2209300 (for *syn-syn*-**BBTB-BODIPY·PhMe-A**), 2209301 (for *syn-syn*-**BBTB-BODIPY·PhMe-B**)</url> contain(s) the supplementary crystallographic data for this paper. These data are

provided free of charge by the joint Cambridge Crystallographic Data Centre and Fachinformationszentrum Karlsruhe <url href=" http://www.ccdc.cam.ac.uk/structures ">Access Structures service</url>.

Photocatalytic reactions: Catalytic reactions were performed using homemade photoreactor, which ensures stable and repeatable conditions.[80] The reactor comprises of aluminium tube (Ø = 150 mm) equipped with 26 W neutral-white light (CIE 1931 (0.38899;0.37837)) LED stripe (54 diodes) and plastic cover containing 8 holes for 4 ml vials allowing for parallelization of the experiment (**Figure S3.6**, SI). The LED stripe was glued inside the tube. To the bottom of the aluminium tube three plastic legs were attached to ensure flow of air. The cover was equipped with a fan (Ø = 60 mm) with air diffusor, while the aluminium tube was cooled by a copper coiled tube heat exchanger sticked to the outside wall of the reactor. Temperature inside reactor was controlled by placing Pt-100 thermometer into one of the reaction vials filled with chloroform. Under such conditions the temperature inside the reactor was maintained at 25 °C. Vials containing 1.5 mL of CHCl$_3$ solutions of 2-furoic acid (12 mg· mL^{-1}; 0.107 M) and **BBTB-BODIPY** (0.05% mol with respect to substrate, 5.4·10^{-5} M) were placed in the photoreactor. The distance from the light source was the same for all samples (25 mm), providing the same irradiance of 1200 W·m^{-2}. The reactor was placed on magnetic stirrer. Each vial was equipped with cross shaped stirrer bars to ensure vigorous stirring. Reaction progress was monitored by ^{1}H NMR spectra analysis of the reaction mixture sampled after a given time. The control experiments show that reaction does not proceed neither in the absence of light nor photocatalyst.

Photocatalytic and hydrolytic stability: Photocatalytic stability was determined with UV-Vis spectroscopy using a Hitachi U-2800 spectrophotometer. Experimental conditions were retained from photocatalytic test reactions. Concordantly, 4 mL vials containing 1.5 mL of CHCl$_3$ solutions of **BBTB-BODIPY** (c = 5.4·10^{-5} M, 1.5 mL) were placed in the photoreactor. Samples were irradiated with 26 W neutral-white light LED strips (irradiance 1200 W·m^{-2}) for 10 h straight. The decomposition process was monitored with UV-Vis spectroscopy with even 1 h time probing period (**Figures S3.1, S3.2**, SI). The parallel experiments were performed without light to determine hydrolytic stability. The half-time of pseudo-first order decomposition of **BBTB-BODIPY** were estimated from the drop in absorption intensity at the absorption maximum wavelength (**Figure S3.3**, SI). The respective values for referential compounds (Rose Bengal and 5,10,15,20-tetraphenylporphyrin) were adopted from our previous studies.[80] The experimental conditions were identical for all referential and studied samples.

Singlet-oxygen generation studies: Singlet-oxygen generation studies were performed using 1,3-diphenylisobenzofuran (DPBF) as a chemical trap in DCM at 10^{-4} M concentration of the **BBTB-BODIPY** photosensitizer. The samples were irradiated with 523 nm Oxxius diode laser (50 mW) light source. Both **BBTB-BODIPY** were stable under experimental conditions as their absorption bands remained unchanged during the experiment (see **Figure S3.5**, SI). The irradiation direction was perpendicular with respect to UV-Vis spectra registration. Whole process was monitored *in situ*. Full UV-Vis spectrum of the mixture was collected in even time periods. Drop in absorbance of the DPBF trap was monitored at 412 nm (DPBF absorption maximum). Methylene Blue (MB) was used as a reference (QY^O = 57%).[164,165] The singlet oxygen quantum yield was calculated by the relative method (3):

$$QY_x^O = QY_r^O \frac{k_x}{k_r} \frac{1-10^{-A_r}}{1-10^{-A_x}} \quad (3)$$

where x and r stays for substance under study and reference, respectively; QY^O is singlet oxygen quantum yield, k denotes rate constant of DPBF reaction with singlet oxygen, A represents the absorbance of the investigated or reference photosensitizer at the excitation wavelength.

[1]   F. Khan, E. Urbonas, D. Volyniuk, J. V. Grazulevicius, S. M. Mobin, R. Misra, *J. Mater. Chem. C* **2020**, *8*, 13375–13388.
[2]   S. Xiang, Z. Huang, S. Sun, X. Lv, L. Fan, S. Ye, H. Chen, R. Guo, L. Wang, *J. Mater. Chem. C* **2018**, *6*, 11436–11443.
[3]   S.-J. Zou, Y. Shen, F.-M. Xie, J.-D. Chen, Y.-Q. Li, J.-X. Tang, *Mater. Chem. Front.* **2020**, *4*, 788–820.
[4]   A. B. Muñoz-García, I. Benesperi, G. Boschloo, J. J. Concepcion, J. H. Delcamp, E. A. Gibson, G. J. Meyer, M. Pavone, H. Pettersson, A. Hagfeldt, M. Freitag, *Chem. Soc. Rev.* **2021**, *50*, 12450–12550.
[5]   L. Mao, Y. Wu, J. Jiang, X. Guo, P. Heng, L. Wang, J. Zhang, *J. Phys. Chem. C* **2020**, *124*, 9233–9242.
[6]   Z.-S. Huang, H. Meier, D. Cao, *J. Mater. Chem. C* **2016**, *4*, 2404–2426.
[7]   J. Gong, K. Sumathy, Q. Qiao, Z. Zhou, *Renew. Sustain. Energy Rev.* **2017**, *68*, 234–246.
[8]   L. Zhang, N. S. Colella, B. P. Cherniawski, S. C. B. Mannsfeld, A. L. Briseno, *ACS Appl. Mater. Interfaces* **2014**, *6*, 5327–5343.
[9]   J.-I. Park, J. W. Chung, J.-Y. Kim, J. Lee, J. Y. Jung, B. Koo, B.-L. Lee, S. W. Lee, Y. W. Jin, S. Y. Lee, *J. Am. Chem. Soc.* **2015**, *137*, 12175–12178.
[10]   M. Iyoda, H. Shimizu, *Chem. Soc. Rev.* **2015**, *44*, 6411–6424.
[11]   A. Mishra, C.-Q. Ma, P. Bäuerle, *Chem. Rev.* **2009**, *109*, 1141–1276.
[12]   D. Joly, P.-A. Bouit, M. Hissler, *J. Mater. Chem. C* **2016**, *4*, 3686–3698.
[13]   M. Stępień, E. Gońka, M. Żyła, N. Sprutta, *Chem. Rev.* **2017**, *117*, 3479–3716.
[14]   T. Baumgartner, F. Jäkle, *Main Group Strategies towards Functional Hybrid Materials*, Wiley, Hoboken, **2018**.
[15]   F. Vidal, F. Jäkle, *Angew. Chem. Int. Ed.* **2019**, *58*, 5846–5870.
[16]   I.Manners, *Synthetic Metal-Containing Polymers,* Wiley-VCH, Weinheim, **2004**.
[17]   A. M. Priegert, B. W. Rawe, S. C. Serin, D. P. Gates, *Chem. Soc. Rev.* **2016**, *45*, 922–953.
[18]   J. K. Salunke, F. L. Wong, K. Feron, S. Manzhos, M. F. Lo, D. Shinde, A. Patil, C. S. Lee, V. A. L. Roy, P. Sonar, P. P. Wadgaonkar, *J. Mater. Chem. C* **2016**, *4*, 1009–1018.
[19]   H. Uoyama, K. Goushi, K. Shizu, H. Nomura, C. Adachi, *Nature* **2012**, *492*, 234–238.
[20]   L. May, T. J. J. Müller, *Chem. – Eur. J.* **2020**, *26*, 12111–12118.
[21]   J. Nau, A. P. W. Schneeweis, T. J. J. Müller, *Mater. Chem. Front.* **2020**, *4*, 621–630.
[22]   J. Nau, V. Brüning, L. Biesen, T. Knedel, C. Janiak, T. J. J. Müller, *Eur. J. Org. Chem.* **2022**, e202101398.
[23]   J. Nau, T. J. J. Müller, *Org. Mater.* **2021**, *3*, 381–389.

[24] L. May, T. J. J. Müller, *Chem. – Eur. J.* **2020**, *26*, 12978–12986.

[25] H. R. V. Berens, K. Mohammad, G. J. Reiss, T. J. J. Müller, *J. Org. Chem.* **2021**, *86*, 8000–8014.

[26] L. May, T. J. J. Müller, *Molecules* **2020**, *25*, 2180.

[27] S. T. Hauer, A. P. W. Schneeweis, S. D. Waniek, L. P. Sorge, K. Heinze, T. J. J. Müller, *Org. Chem. Front.* **2021**, *8*, 5744–5755.

[28] A. P. W. Schneeweis, S. T. Hauer, G. J. Reiss, T. J. J. Müller, *Chem. – Eur. J.* **2019**, *25*, 3582–3590.

[29] X. Su, T. A. Bartholome, J. R. Tidwell, A. Pujol, S. Yruegas, J. J. Martinez, C. D. Martin, *Chem. Rev.* **2021**, *121*, 4147–4192.

[30] S. Fuchs, A. Jayaraman, I. Krummenacher, L. Haley, M. Baštovanović, M. Fest, K. Radacki, H. Helten, H. Braunschweig, *Chem. Sci.* **2022**, *13*, 2932–2938.

[31] K. Schickedanz, J. Radtke, M. Bolte, H.-W. Lerner, M. Wagner, *J. Am. Chem. Soc.* **2017**, *139*, 2842–2851.

[32] J. He, F. Rauch, A. Friedrich, J. Krebs, I. Krummenacher, R. Bertermann, J. Nitsch, H. Braunschweig, M. Finze, T. B. Marder, *Angew. Chem. Int. Ed.* **2021**, *60*, 4833–4840.

[33] T. Doan, A. Chardon, A. Osi, D. Mahaut, N. Tumanov, J. Wouters, B. Champagne, G. Berionni, *Chem. – Eur. J.* **2021**, *27*, 1736–1743.

[34] S. Kirschner, I. Uecker, M. Bolte, H.-W. Lerner, M. Wagner, *Organometallics* **2019**, *38*, 2818–2823.

[35] A. John, M. Bolte, H.-W. Lerner, M. Wagner, *Angew. Chem. Int. Ed.* **2017**, *56*, 5588–5592.

[36] V. M. Hertz, M. Bolte, H.-W. Lerner, M. Wagner, *Angew. Chem. Int. Ed.* **2015**, *54*, 8800–8804.

[37] R. J. Kahan, D. L. Crossley, J. Cid, J. E. Radcliffe, A. W. Woodward, V. Fasano, S. Endres, G. F. S. Whitehead, M. J. Ingleson, *Chem. Commun.* **2018**, *54*, 9490–9493.

[38] A. John, M. Bolte, H.-W. Lerner, G. Meng, S. Wang, T. Peng, M. Wagner, *J. Mater. Chem. C* **2018**, *6*, 10881–10887.

[39] R. R. Cloke, T. Marangoni, G. D. Nguyen, T. Joshi, D. J. Rizzo, C. Bronner, T. Cao, S. G. Louie, M. F. Crommie, F. R. Fischer, *J. Am. Chem. Soc.* **2015**, *137*, 8872–8875.

[40] J. M. Farrell, C. Mützel, D. Bialas, M. Rudolf, K. Menekse, A.-M. Krause, M. Stolte, F. Würthner, *J. Am. Chem. Soc.* **2019**, *141*, 9096–9104.

[41] S. K. Mellerup, S. Wang, *Trends Chem.* **2019**, *1*, 77–89.

[42] C. Dou, S. Saito, K. Matsuo, I. Hisaki, S. Yamaguchi, *Angew. Chem. Int. Ed.* **2012**, *51*, 12206–12210.

[43] X. Yin, J. Liu, F. Jäkle, *Chem. – Eur. J.* **2021**, *27*, 2973–2986.

[44] G. Liao, X. Chen, Y. Qiao, K. Liu, N. Wang, P. Chen, X. Yin, *Org. Lett.* **2021**, *23*, 5836–5841.

[45] S. Yamaguchi, T. Shirasaka, S. Akiyama, K. Tamao, *J. Am. Chem. Soc.* **2002**, *124*, 8816–8817.

[46] T. Agou, J. Kobayashi, T. Kawashima, *Inorg. Chem.* **2006**, *45*, 9137–9144.

[47] M. Melaïmi, S. Solé, C.-W. Chiu, H. Wang, F. P. Gabbaï, *Inorg. Chem.* **2006**, *45*, 8136–8143.

[48] C. R. Wade, A. E. J. Broomsgrove, S. Aldridge, F. P. Gabbaï, *Chem. Rev.* **2010**, *110*, 3958–3984.

[49] E. von Grotthuss, A. John, T. Kaese, M. Wagner, *Asian J. Org. Chem.* **2018**, *7*, 37–53.

[50] E. Dimitrijević, M. S. Taylor, *Chem. Sci.* **2013**, *4*, 3298–3303.

[51] S. N. Kessler, H. A. Wegner, *Org. Lett.* **2010**, *12*, 4062–4065.

[52] S. N. Kessler, M. Neuburger, H. A. Wegner, *Eur. J. Org. Chem.* **2011**, 3238–3245.

[53] S. Ahles, S. Götz, L. Schweighauser, M. Brodsky, S. N. Kessler, A. H. Heindl, H. A. Wegner, *Org. Lett.* **2018**, *20*, 7034–7038.

[54] L. Schweighauser, I. Bodoky, S. N. Kessler, D. Häussinger, C. Donsbach, H. A. Wegner, *Org. Lett.* **2016**, *18*, 1330–1333.

[55] S. N. Kessler, M. Neuburger, H. A. Wegner, *J. Am. Chem. Soc.* **2012**, *134*, 17885–17888.

[56] S. Beeck, S. Ahles, H. A. Wegner, *Chem. – Eur. J.* **2022**, *28*, e202104085.

[57] M. A. Strauss, D. Kohrs, J. Ruhl, H. A. Wegner, *Eur. J. Org. Chem.* **2021**, *2021*, 3866–3873.

[58] M. Balkenhohl, H. Jangra, T. Lenz, M. Ebeling, H. Zipse, K. Karaghiosoff, P. Knochel, *Angew. Chem. Int. Ed.* **2019**, *58*, 9244–9247.

[59] L. Schweighauser, H. A. Wegner, *Chem. - Eur. J.* **2016**, *22*, 14094–14103.

[60] Z. Lu, L. Schweighauser, H. Hausmann, H. A. Wegner, *Angew. Chem. Int. Ed.* **2015**, *54*, 15556–15559.

[61] S. S. Kothavale, J. Y. Lee, *Adv. Opt. Mater.* **2020**, *8*, 2000922.

[62] H. Lee, D. Karthik, R. Lampande, J. H. Ryu, J. H. Kwon, *Front. Chem.* **2020**, *8*, 373.

[63] M. Godumala, S. Choi, M. J. Cho, D. H. Choi, *J. Mater. Chem. C* **2016**, *4*, 11355–11381.

[64] I. S. Park, K. Matsuo, N. Aizawa, T. Yasuda, *Adv. Funct. Mater.* **2018**, *28*, 1802031.

[65] Z. Yang, Z. Mao, Z. Xie, Y. Zhang, S. Liu, J. Zhao, J. Xu, Z. Chi, M. P. Aldred, *Chem. Soc. Rev.* **2017**, *46*, 915–1016.

[66] Y. Li, X. Chen, W. Zhang, J. Zhang, L. Xu, Y. Qiao, K. Liu, N. Wang, P. Chen, X. Yin, *Org. Lett.* **2021**, *23*, 7236–7241.

[67] L. Ji, S. Griesbeck, T. B. Marder, *Chem. Sci.* **2017**, *8*, 846–863.

[68] V. D. Romanenko, J.-M. Sotiropoulos, *Compr. Heterocycl. Chem. IV*, Elsevier, **2022**, p. 806–845.

[69] A. Dhiman, L. Giribabu, R. Trivedi, *Chem. Rec.* **2021**, *21*, 1738–1770.

[70] A. Iida, S. Yamaguchi, *J. Am. Chem. Soc.* **2011**, *133*, 6952–6955.

[71] L. G. Mercier, W. E. Piers, R. W. Harrington, W. Clegg, *Organometallics* **2013**, *32*, 6820–6826.

[72] S. Sa, A. C. Murali, P. Nayak, K. Venkatasubbaiah, *Chem. Commun.* **2021**, *57*, 10170–10173.

[73] D. R. Levine, M. A. Siegler, J. D. Tovar, *J. Am. Chem. Soc.* **2014**, *136*, 7132–7139.

[74] Y. Adachi, J. Ohshita, *Organometallics* **2018**, *37*, 869–881.

[75] Y. Adachi, F. Arai, M. Sakabe, J. Ohshita, *Polym. Chem.* **2021**, *12*, 3471–3477.

[76] D. R. Levine, R. E. Messersmith, M. A. Siegler, J. D. Tovar, *Can. J. Chem.* **2017**, *95*, 381–389.

[77] Y. Adachi, F. Arai, K. Yamada, M. Kurihara, J. Ohshita, *Organometallics* **2022**, *41*, 1225–1231.

[78] Y. Yan, Z. Sun, C. Li, J. Zhang, L. Lv, X. Liu, X. Liu, *Asian J. Org. Chem.* **2017**, *6*, 496–502.

[79] K. Durka, I. Głowacki, S. Luliński, B. Łuszczyńska, J. Smętek, P. Szczepanik, J. Serwatowski, U. E. Wawrzyniak, G. Wesela-Bauman, E. Witkowska, G. Wiosna-Sałyga, K. Woźniak, *J. Mater. Chem. C* **2015**, *3*, 1354–1364.

[80] P. H. Marek-Urban, M. Urban, M. Wiklińska, K. Paplińska, K. Woźniak, A. Blacha-Grzechnik, K. Durka, *J. Org. Chem.* **2021**, *86*, 12714–12722.

[81] M. A. Filatov, S. Karuthedath, P. M. Polestshuk, H. Savoie, K. J. Flanagan, C. Sy, E. Sitte, M. Telitchko, F. Laquai, R. W. Boyle, M. O. Senge, *J. Am. Chem. Soc.* **2017**, *139*, 6282–6285.

[82] M. A. Filatov, S. Karuthedath, P. M. Polestshuk, S. Callaghan, K. J. Flanagan, M. Telitchko, T. Wiesner, F. Laquai, M. O. Senge, *Phys. Chem. Chem. Phys.* **2018**, *20*, 8016–8031.

[83] M. A. Filatov, *Org. Biomol. Chem.* **2020**, *18*, 10–27.

[84] A. A. Ghogare, A. Greer, *Chem. Rev.* **2016**, *116*, 9994–10034.

[85] D. M. Schultz, T. P. Yoon, *Science* **2014**, *343*, 1239176.

[86] J. P. Celli, B. Q. Spring, I. Rizvi, C. L. Evans, K. S. Samkoe, S. Verma, B. W. Pogue, T. Hasan, *Chem. Rev.* **2010**, *110*, 2795–2838.

[87] X. Li, S. Kolemen, J. Yoon, E. U. Akkaya, *Adv. Funct. Mater.* **2017**, *27*, 1604053.

[88] M. DeRosa, *Coord. Chem. Rev.* **2002**, 351–371.

[89] D. K. Mai, C. Kim, J. Lee, T. P. Vales, I. W. Badon, K. De, S. Cho, J. Yang, H.-J. Kim, *Sci. Rep.* **2022**, *12*, 2541.

[90] W. Li, J. Zhang, Z. Gao, J. Qi, D. Ding, *Coord. Chem. Rev.* **2022**, *471*, 214754.

[91] E. Bassan, A. Gualandi, P. G. Cozzi, P. Ceroni, *Chem. Sci.* **2021**, *12*, 6607–6628.

[92] V.-N. Nguyen, Y. Yan, J. Zhao, J. Yoon, *Acc. Chem. Res.* **2021**, *54*, 207–220.

[93] A. A. Cullen, A. Rajagopal, K. Heintz, A. Heise, R. Murphy, I. V. Sazanovich, G. M. Greetham, M. Towrie, C. Long, D. Fitzgerald-Hughes, M. T. Pryce, *J. Phys. Chem. B* **2021**, *125*, 1550–1557.

[94] D. O. Frimannsson, M. Grossi, J. Murtagh, F. Paradisi, D. F. O'Shea, *J. Med. Chem.* **2010**, *53*, 7337–7343.

[95] E. Caruso, S. Banfi, P. Barbieri, B. Leva, V. T. Orlandi, *J. Photochem. Photobiol. B* **2012**, *114*, 44–51.

[96] K. R. Stoll, F. Scholle, J. Zhu, X. Zhang, R. A. Ghiladi, *Photochem. Photobiol. Sci.* **2019**, *18*, 1923–1932.

[97] W. J. Peveler, S. Noimark, H. Al-Azawi, G. B. Hwang, C. R. Crick, E. Allan, J. B. Edel, A. P. Ivanov, A. J. MacRobert, I. P. Parkin, *ACS Appl. Mater. Interfaces* **2018**, *10*, 98–104.

[98] A. Atilgan, Y. Beldjoudi, J. Yu, K. O. Kirlikovali, J. A. Weber, J. Liu, D. Jung, P. Deria, T. Islamoglu, J. F. Stoddart, O. K. Farha, J. T. Hupp, *ACS Appl. Mater. Interfaces* **2022**, *14*, 12596–12605.

[99] H. Wang, G. W. Wagner, A. X. Lu, D. L. Nguyen, J. H. Buchanan, P. M. McNutt, C. J. Karwacki, *ACS Appl. Mater. Interfaces* **2018**, *10*, 18771–18777.

[100] S. Shah, A. Bajaj, A. Shibu, Md. E. Ali, P. P. Neelakandan, *Chem. – Eur. J.* **2018**, *24*, 18788–18794.

[101] H. Kim, W. Kim, Y. Mackeyev, G.-S. Lee, H.-J. Kim, T. Tachikawa, S. Hong, S. Lee, J. Kim, L. J. Wilson, T. Majima, P. J. J. Alvarez, W. Choi, J. Lee, *Environ. Sci. Technol.* **2012**, *46*, 9606–9613.

[102] H. R. V. Berens, T. J. J. Müller, *Org. Mater.* **2021**, *3*, 155–167.

[103] S. Winstein, P. Carter, F. A. L. Anet, A. J. R. Bourn, *J. Am. Chem. Soc.* **1965**, *87*, 5247–5249.

[104] Z. Zeng, G. Kociok-Köhn, T. J. Woodman, M. G. Rowan, I. S. Blagbrough, *ACS Omega* **2021**, *6*, 12769–12786.

[105] R. F. W. Bader, *Atoms in Molecules: A Quantum Theory; International Series of Monographs on Chemistry,* Oxford University Press, Oxford, New York*,* **1994**.

[106] S. P. Thomas, A. G. Dikundwar, S. Sarkar, M. S. Pavan, R. Pal, V. R. Hathwar, T. N. G. Row, *Molecules* **2022**, *27*, 3690.

[107] M. Bai, S. P. Thomas, R. Kottokkaran, S. K. Nayak, P. C. Ramamurthy, T. N. Guru Row, *Cryst. Growth Des.* **2014**, *14*, 459–466.

[108] K. Durka, S. Gontarczyk, S. Luliński, J. Serwatowski, K. Woźniak, *Cryst. Growth Des.* **2016**, *16*, 4292–4308.

[109] W. Zeng, S. Gong, C. Zhong, C. Yang, *J. Phys. Chem. C* **2019**, *123*, 10081–10086.

[110] M. Urban, K. Durka, P. Górka, G. Wiosna-Sałyga, K. Nawara, P. Jankowski, S. Luliński, *Dalton Trans.* **2019**, *48*, 8642–8663.

[111] K. Yuan, X. Wang, S. K. Mellerup, I. Kozin, S. Wang, *J. Org. Chem.* **2017**, *82*, 13481–13487.

[112] A. Loudet, K. Burgess, *Chem. Rev.* **2007**, *107*, 4891–4932.

[113] M. L. Agazzi, M. B. Ballatore, A. M. Durantini, E. N. Durantini, A. C. Tomé, *J. Photochem. Photobiol. C Photochem. Rev.* **2019**, *40*, 21–48.

[114] F. Würthner, T. E. Kaiser, C. R. Saha-Möller, *Angew. Chem. Int. Ed.* **2011**, *50*, 3376–3410.

[115] D. Möbius, *Adv. Mater.* **1995**, *7*, 437–444.

[116] J. Mei, N. L. C. Leung, R. T. K. Kwok, J. W. Y. Lam, B. Z. Tang, *Chem. Rev.* **2015**, *115*, 11718–11940.

[117] Y. Hong, J. W. Y. Lam, B. Z. Tang, *Chem. Commun.* **2009**, 4332.

[118] A. I. Rodrigues, C. A. Figueira, C. S. B. Gomes, D. Suresh, B. Ferreira, R. E. Di Paolo, D. de S. Pereira, F. B. Dias, M. J. Calhorda, J. Morgado, A. L. Maçanita, P. T. Gomes, *Dalton Trans.* **2019**, *48*, 13337–13352.

[119] L. Huang, J. Zhao, S. Guo, C. Zhang, J. Ma, *J. Org. Chem.* **2013**, *78*, 5627–5637.

[120] W. Jentzen, X.-Z. Song, J. A. Shelnutt, *J. Phys. Chem. B,* **1997**, *101*, 1684–1699.

[121] F. Wilkinson, P. Helman, A. B. Ross, J. Phys. Chem. Ref. Data **1993**, *22*, 113-262.

[122] W. Hu, M. Liu, X.-F. Zhang, M. Shi, M. Jia, X. Hu, L. Liu, T. Wang, *J. Phys. Chem. C* **2020**, *124*, 23558–23566.

[123] V.-N. Nguyen, J. Ha, C. W. Koh, B. Ryu, G. Kim, J. H. Park, C.-Y. Kim, S. Park, J. Yoon, *Chem. Mater.* **2021**, *33*, 7889–7896.

[124] Y. Dong, M. Taddei, S. Doria, L. Bussotti, J. Zhao, G. Mazzone, M. Di Donato, *J. Phys. Chem. B* **2021**, *125*, 4779–4793.

[125] T. Maki, Z. Zhou, Y. Irie, T. Matsunaga, T. Onodera, S. Imamichi, Y. Sasaki, M. Masutani, H. Otaki, E. Sakuda, Y. Tanaka, H. Murota, *Dyes Pigments* **2023**, *210*, 110963.

[126] J. Miao, Y. Huo, G. Yao, Y. Feng, J. Weng, W. Zhao, W. Guo, *Angew. Chem. Int. Ed.* **2022**, *61*, e202201815.

[127] X. Zhang, Z. Wang, Y. Hou, Y. Yan, J. Zhao, B. Dick, *J. Mater. Chem. C* **2021**, *9*, 11944–11973.

[128] Z. Wang, J. Zhao, M. Di Donato, G. Mazzone, *Chem. Commun.* **2019**, *55*, 1510–1513.

[129] Y. Dong, A. A. Sukhanov, J. Zhao, A. Elmali, X. Li, B. Dick, A. Karatay, V. K. Voronkova, *J. Phys. Chem. C* **2019**, *123*, 22793–22811.

[130] Z. Wang, A. A. Sukhanov, A. Toffoletti, F. Sadiq, J. Zhao, A. Barbon, V. K. Voronkova, B. Dick, *J. Phys. Chem. C* **2019**, *123*, 265–274.

[131] Y. Dong, A. Elmali, J. Zhao, B. Dick, A. Karatay, *ChemPhysChem* **2020**, *21*, 1388–1401.

[132] Z. Wang, M. Ivanov, Y. Gao, L. Bussotti, P. Foggi, H. Zhang, N. Russo, B. Dick, J. Zhao, M. Di Donato, G. Mazzone, L. Luo, M. Fedin, *Chem. – Eur. J.* **2020**, *26*, 1091–1102.

[133] M. Imran, A. M. El-Zohry, C. Matt, M. Taddei, S. Doria, L. Bussotti, P. Foggi, J. Zhao, M. Di Donato, O. F. Mohammed, S. Weber, *J. Mater. Chem. C* **2020**, *8*, 8305–8319.

[134] S. Callaghan, B. E. Vindstad, K. J. Flanagan, T. B. Melø, M. Lindgren, K. Grenstad, O. A. Gederaas, M. O. Senge, *ChemPhotoChem* **2021**, *5*, 131–141.

[135] J. T. Buck, A. M. Boudreau, A. DeCarmine, R. W. Wilson, J. Hampsey, T. Mani, *Chem* **2019**, *5*, 138–155.

[136] Z. Wang, J. Zhao, *Org. Lett.* **2017**, *19*, 4492–4495.

[137] Y. Hou, Q. Liu, J. Zhao, *Chem. Commun.* **2020**, *56*, 1721–1724.

[138] Y. Hou, I. Kurganskii, A. Elmali, H. Zhang, Y. Gao, L. Lv, J. Zhao, A. Karatay, L. Luo, M. Fedin, *J. Chem. Phys.* **2020**, *152*, 114701.

[139] K. Chen, M. Taddei, L. Bussotti, P. Foggi, J. Zhao, M. Di Donato, *ChemPhotoChem* **2020**, *4*, 487–501.

[140] F. B. Dias, J. Santos, D. R. Graves, P. Data, R. S. Nobuyasu, M. A. Fox, A. S. Batsanov, T. Palmeira, M. N. Berberan-Santos, M. R. Bryce, A. P. Monkman, *Adv. Sci.* **2016**, *3*, 1600080.

[141] C. Würth, M. Grabolle, J. Pauli, M. Spieles, U. Resch-Genger, *Nat. Protoc.* **2013**, *8*, 1535–1550.

[142] U. Resch-Genger, K. Rurack, *Pure Appl. Chem.* **2013**, *85*, 2005–2013.

[143] K. Suzuki, A. Kobayashi, S. Kaneko, K. Takehira, T. Yoshihara, H. Ishida, Y. Shiina, S. Oishi, S. Tobita, *Phys. Chem. Chem. Phys.* **2009**, *11*, 9850–9860.

[144] J. Shen, R. D. Snook, *Chem. Phys. Lett.* **1989**, *155*, 583–586.

[145] J. C. de Mello, H. F. Wittmann, R. H. Friend, *Adv. Mater.* **1997**, *9*, 230–232.

[146] P. Pander, P. Data, F. B. Dias, *J. Vis. Exp.* **2018**, 56614.

[147] M. J. Frisch, G. W. Trucks, H. B. Schlegel, G. E. Scuseria, M. A. Robb, J. R. Cheeseman, G. Scalmani, V. Barone, G. A. Petersson, H. Nakatsuji, X. Li, M. Caricato, A. V. Marenich, J. Bloino, B. G. Janesko, R. Gomperts, B. Mennucci, H. P. Hratchian, J. V. Ortiz, A. F. Izmaylov, J. L. Sonnenberg, D. Williams-Young, F. Ding, F. Lipparini, F. Egidi, J. Goings, B. Peng, A. Petrone, T. Henderson, D. Ranasinghe, V. G. Zakrzewski, J. Gao, N. Rega, G. Zheng, W. Liang, M. Hada, M. Ehara, K. Toyota, R. Fukuda, J. Hasegawa, M. Ishida, T. Nakajima, Y. Honda, O. Kitao, H. Nakai, T. Vreven, K. Throssell, J. A. Montgomery, Jr., J. E. Peralta, F. Ogliaro, M. J. Bearpark, J. J. Heyd, E. N. Brothers, K. N. Kudin, V. N. Staroverov, T. A. Keith, R. Kobayashi, J. Normand, K. Raghavachari, A. P. Rendell, J. C. Burant, S. S. Iyengar, J. Tomasi, M. Cossi, J. M. Millam, M. Klene, C. Adamo, R. Cammi, J. W. Ochterski, R. L. Martin, K. Morokuma, O. Farkas, J. B. Foresman, and D. J. Fox, *Gaussian 16, Revision C.01, Gaussian, Inc.,* Wallingford CT, **2016**.

[148] Y. Zhao, D. G. Truhlar, *Theor. Chem. Acc.* **2008**, *120*, 215–241.

[149] C. Lee, W. Yang, R. G. Parr, *Phys. Rev. B* **1988**, *37*, 785–789.

[150] A. D. Becke, *J. Chem. Phys.* **1993**, *98*, 5648–5652.

[151] Todd A. Keith, *AIMAll (Version 19.10.12),* TK Gristmill Software, Overland Park KS, USA, **2019**.

[152] P. von R. Schleyer, C. Maerker, A. Dransfeld, H. Jiao, N. J. R. van Eikema Hommes, *J. Am. Chem. Soc.* **1996**, *118*, 6317–6318.

[153] J. Tomasi, B. Mennucci, R. Cammi, *Chem. Rev.* **2005**, *105*, 2999–3094.

[154] R. L. Martin, *J. Chem. Phys.* **2003**, *118*, 4775–4777.

[155] *Avogadro: An Open-Source Molecular Builder and Visualization Tool. Version 1.2.0. Http://Avogadro.Cc/, J. Cheminformatics,* **2012***, 4*, 17.

[156] H. F. Higginbotham, M. Czichy, B. K. Sharma, A. M. Shaikh, R. M. Kamble, P. Data, *Electrochimica Acta* **2018**, *273*, 264–272.

[157] X. Li, R. Tang, K. Hu, L. Zhang, Z. Ding, *Electrochimica Acta* **2016**, *210*, 734–742.

[158] C. M. Cardona, W. Li, A. E. Kaifer, D. Stockdale, G. C. Bazan, *Adv. Mater.* **2011**, *23*, 2367–2371.

[159] J.-L. Bredas, *Mater Horiz* **2014**, *1*, 17–19.

[160] *Rigaku Oxford Diffraction, "Crysalis Pro" v. 1.171.38.46,* **2018**.

[161] G. M. Sheldrick, *Acta Crystallogr. Sect. Found. Adv.* **2015**, *71*, 3–8.

[162] G. M. Sheldrick, *Acta Crystallogr. Sect. C Struct. Chem.* **2015**, *71*, 3–8.

[163] O. V. Dolomanov, L. J. Bourhis, R. J. Gildea, J. A. K. Howard, H. Puschmann, *J. Appl. Crystallogr.* **2009**, *42*, 339–341.

[164] W. Li, L. Li, H. Xiao, R. Qi, Y. Huang, Z. Xie, X. Jing, H. Zhang, *RSC Adv.* **2013**, *3*, 13417–13421.

[165] N. Epelde-Elezcano, V. Martínez-Martínez, E. Peña-Cabrera, C. F. A. Gómez-Durán, I. L. Arbeloa, S. Lacombe, *RSC Adv.* **2016**, *6*, 41991–41998.

Entry for the Table of Contents

15

We present synthesis and physicochemical studies of two regioisomeric π-electron extended [1,4]thiaborins annulated with two benzothiophene units. They were used as scaffolds for construction of thiaborin-based BODIPY singlet-oxygen photosensitizers with evident potential for use as photocatalysts.